Materials Science in Semiconductor Processing 152 (2022) 107081

Contents lists available at ScienceDirect

Materials Science in Semiconductor Processing

journal homepage: www.elsevier.com/locate/mssp

Structural, elastic, electronic, optical and thermoelectric response of lead-free double perovskite Rb_2TlInX_6 (X=Cl, I) for energy storage devices: DFT+SOC investigations

Moeen Ud Din [a], Quratul Ain [b], Masood Yousaf [c], Junaid Munir [a,*]

[a] Department of Physics, Riphah International University, Lahore, Pakistan
[b] Department of Physics, University of Management and Technology, Lahore, Pakistan
[c] Department of Physics, University of Education, Lahore, Pakistan

ARTICLE INFO

Keywords:
Double perovskites
Density functional theory
Spin- orbit coupling
Elastic properties
Electronic properties
Optical properties
BoltzTraP code

ABSTRACT

Double perovskites Rb_2TlInX_6 (X = Cl, I) have been simulated with the help of density functional theory to determine their structural, elastic, electronic, optical and thermal properties. The full-potential linearized augmented plane wave (FP-LAPW) method is used through the WIEN2K code. Exchange-correlation potential is described by using the well-organized modified Becke-Johnson (mBJ) with the combination of spin-orbit coupling (SOC). Structural optimization and formation energy calculations justify the stability of both compounds. The elastic parameters are calculated to measure the mechanical stuff, such as shear modulus (G), Poisson ratio (ν) and anisotropic factor (A). The studied compounds showing semiconductor nature with a bandgap of 3.51eV and 3.47eV for $Rb_2TlInCl_6$ and 1.43eV and 1.40eV for Rb_2TlInI_6 with mBJ and mBJ+SOC potentials, respectively. The density of states also exposes the bandgap and semiconductor nature of the materials. The optical properties of the compounds have been examined in terms of the dielectric function, refractive index, absorption, reflection, and energy loss. We also investigated the temperature-dependent transport parameters for both compounds. High electrical and low thermal conductivity with good ZT values for both materials make them potential candidates for thermoelectric applications.

1. Introduction

The industrial and technological demand for advanced materials with novel properties invokes the scientific community to understand the periodic table elements and their combinations thoroughly. Over time, researchers are uncovering new materials and these materials have the potential to meet today's technological challenges. As a result, the material world sees significant shifts in the imaginative design of novel materials. In recent years, a significant rise in computational power combined with mathematical breakthroughs in quantum mechanics has made it possible to conduct well-defined and precise quantum-based calculations. Consequently, the computational power has been increased to such an extent that the characteristics of materials that were earlier immensely tough to examine are now comfortably estimated with high precision [1,2]. Due to the wide range of technological applications and multifunctional properties, research on perovskites, particularly on double perovskites has intensified in the last few years [3–7]. Lead-based halide perovskites have faced stability problems in their applications due to temperature sensitivity, moisture and the existence of toxic lead. To reduce these problems, the lead-free metal halide perovskites having the required absorption capacity were designed. The replacement of Pb^{2+} by isovalent Sn^{2+} and Ge^{2+}, which can be easily oxidized to Sn^{4+} and Ge^{4+5}, results in instability [8]. In their alternative, Pb^{2+} can be replaced by monovalent B^{+} and a trivalent B^{3+}, to form the desired double perovskites [9]. The general formula of perovskites is ABX_3, where A and B are cations and X is an anion. The charge of sites A and B can vary. The material community has benefited from double perovskite compounds with the general formula $A_2BB'X_6$, which have a wide range of technological applications, including insulating ferrimagnetism, half-metallic, spintronic, magneto-dielectric, ferromagnetic, multi-ferroic, and magneto-optic materials among others [10–15]. A large number of studies on halide perovskites for solar cell applications have also been reported, such as $MAPbBr_3$ and $MAPbI_3$ [16–19]. Perovskites with ABX_3 structure, such as $BaPuO_3$, $SrAmO_3$,

* Corresponding author.
E-mail address: junaid_ij2000@yahoo.com (J. Munir).

https://doi.org/10.1016/j.mssp.2022.107081
Received 11 May 2022; Received in revised form 11 August 2022; Accepted 26 August 2022

$BaAmO_3$, $EuGaO_3$, $SrPuO_3$, and $EuInO_3$ are reported for spintronic applications [20–23]. The family of double perovskites reveal a broad range of magnetic behavior including antiferromagnets (Ba_2LiOsO_6), ferromagnetism (Ba_2MgReO_6, Ba_2NaOsO_6), spin-singlet ground states for (Ba_2YMoO_6) and spin glasses (Sr_2CaReO_6) [24–28]. The Rb_2NaCoF_6 [29] shows a non-magnetic behavior having a wide range of potential for high class ultraviolet thin-film devices. Recently, perovskites like $BaMoO_3$, $SrMoO_3$, $XReO_3$ (X = Rb, Cs, Tl), $SnTaO_3$, $PbMoO_3$ are reported for fuel cell potential applications [30–33]. Cubic double perovskites Rb_2TlInX_6 (X = Cl, I) have recently been introduced with the space group of Fm $\bar{3}$ m (225) [34,35]. Several more double perovskites of the type $A_2BB'O_6$ have also been identified, and they are being investigated for use in electrical and magnetic applications as well as thermoelectric, mechanical, thermodynamic and optical applications [35–41]. The first-principles calculations have been done on several double perovskite halides to study their structural, elastic and optoelectronic properties [42–44]. In the present work, we report two important members of the double perovskite family, i.e., $Rb_2TlInCl_6$ and Rb_2TlInI_6. According to the author's best knowledge, so far, no literature is available to explore the physical properties of these materials. So an attempt has been made in the present investigation to forecast the properties of these double perovskites as well as to investigate their prospective uses. The most successful density functional theory has been used to explore the behavior of studied compounds in terms of structural, electronic, optical and transport properties.

2. Computational method

Various approaches to solving the DFT equations are too complex and not to be determined here. The computation of pseudo potentials using the plane wave (PW) technique has resulted in the linearized augmented plane wave (LAPW) method, which is the most explicit course of action and hence the subject of the current work. The structural, electronic band profile and optical properties of the materials are evaluated by using the wien2k modelling tool [45]. Through the iterative method, the solution of Kohn-Sham equation is achieved, which gives more accurate and precise results for the ground state properties. Precisely, the single undetermined term exchange-correlation potential in current formulism is approximated by applying generalized gradient approximation (GGA) and modified Becke-Johnson (mBJ) potential [46, 47].

$$E_{xc}^{GGA} = \int \rho(r)\varepsilon_x^{hom}(\rho(r))F_{xc}(\rho(r),\ \nabla\rho(r))dr \tag{1}$$

Where F_{xc} is the dimensionless factor and ϵ_x^{hom} is the exchange energy of the homogeneous system. The GGA approach does not estimate highly coupled electron systems, such as transition metal (TM) complexes with d and f-states. The occupancy of d-states raises the effect of the exchange-correlation. Thus, the modified Becke- Johnson (mBJ) is used which is suggested by Trans and Blaha [48].

$$\nu_x^{mBJ}(r) = c\nu_x^{Br}(r) + (3(-2))\frac{1}{\pi}\sqrt{\frac{5}{12}}\sqrt{\frac{2t(r)}{\rho(r)}} \tag{2}$$

Where $\nu_x^{mBJ}(r)$ is Becke-Roussel's (BR) potential for bulk crystalline.

During the calculations, the volume of a unit cell is divided into atomic-like muffin tin spheres, where the wave function exhibits atomic characteristics and interstitial region. In the interstitial zone, plane waves provide an extended potential in the muffin tin region and spherical harmonics create a standard basis set. The potential in both regions is expressed as,

$$V(\boldsymbol{r}) = \begin{cases} \sum_G V_{MT}^L(r)Y_L(\hat{\boldsymbol{r}}) & muffin-tin\ region \\ \sum_K V_I^G e^{iGr} & interstitial\ region \end{cases} \tag{3}$$

The basis set's expansion is regulated by the RMT $K_{max} = 7$ and $l_{max} = 10$ criteria, where RMT represents the minimum muffin tin radii and K_{max} represents the most significant value of K. When attempting to achieve the convergence, the partitioned of the unit cell is done in the k-space by using a dense mesh of 1500-k points over the Brillouin zone. Charge convergence between successive cycles is improved by iterating up to 0.0001e and energy convergence up to 0.0001Ry. The thermoelectric properties are determined under the relaxation time (τ) constant approximation by using the BoltzTtraP code [49].

The optical properties such as dielectric function $\varepsilon(\omega)$, refractive index $\eta(\omega)$, reflectivity $R(\omega)$, optical loss $L(\omega)$ and absorption coefficient $\alpha(\omega)$ are also calculated which can be determined by the following relations:

$$\varepsilon(\omega) = \varepsilon_1(\omega) + i\varepsilon_2(\omega) \tag{4}$$

Where

$$\varepsilon_1(\omega) = 1 + \frac{2p}{\pi}\int_0^\infty \frac{\omega'\varepsilon_2(\omega')}{\omega'^2 - \omega^2}d\omega' \tag{5}$$

$$\varepsilon_2(\omega) = \frac{8}{2\pi\omega^2}\sum_{nn'}\int |p_{nn'}|^2\frac{dS_k}{\nabla\omega_{nn'}(k)} \tag{6}$$

Where $P_{nn'}(k)$ is dipole matrix element, $\omega_{nn'}(k)$ is energy difference, S_k is surface energy, and P is Cauchy principle.

The refractive index can be determined as;

$$\eta(\omega) = \frac{\sqrt{\varepsilon_1^2(\omega) + \varepsilon_2^2(\omega)}\varepsilon_1(\omega)^{\frac{1}{2}}}{\sqrt{2}} \tag{7}$$

The reflectivity is given as;

$$R(\omega) = \frac{\eta - 1^2 + k^2}{\eta + 1^2 + k^2} \tag{8}$$

The energy loss function is presented with the following equation;

$$L(\omega) = \frac{\varepsilon_2(\omega)}{[\varepsilon_1^2(\omega) + \varepsilon_2^2(\omega)]} \tag{9}$$

The absorption coefficient is presented as:

$$\alpha(\omega) = \sqrt{2\omega}\left[\sqrt{\varepsilon_1^2(\omega) + \varepsilon_2^2(\omega) - \varepsilon_1(\omega)}\right]^{\frac{1}{2}} \tag{10}$$

To evaluate the semi-classic transport properties of the studied materials BoltzTraP code is used. By using this analytical representation, we calculate the transport distribution with the help of necessary derivatives. This method is very convincing agreement compared to earlier calculations, which in principle should be exact within Boltzmann theory. The BoltzTraP [50] code using constant relaxation time (τ) approximations for the charge carriers is employed. At absolute temperature T, the thermal (K_e) and electrical conductivity (σ), and the Seebeck coefficient (S) are calculated while taking the relaxation time as constant during the calculations.

3. Results and discussion

3.1. Structural properties

The double perovskites Rb_2TlInX_6 (X = Cl, I) exhibit a cubic phase in $Fm\bar{3}m$ space group symmetry with lattice constants of 11.20 Å and 12.50 Å, respectively. The Rb atoms are located at the position 8c (1/4, 1/4, 1/

4), Tl at 4b (1/2, 0, 0), In at 4a (0, 0, 0) and Cl and I atoms are sited at 24e (X, 0, 0) (where X = 0.23,0.26). The arrangement of cations and anions predominately determines the materials' structural stability, band structure, and their particular application to great coverage. The structural optimization and geometry have been performed in a non-magnetic (NM) phase. Based on Birch Murnaghan's equation of state, the optimized volume for studied compounds is calculated by fitting the total energy as a function of the cell volume [51–53]. The ground state energy is found lowest energy for both compounds and thus a stable configuration is achieved.

$$E(V) = E_o + \frac{9B_oV_o}{16}\left\{\left[\left(\frac{V_o}{V}\right)^{2/3} - 1\right]B_o' + \left[\left(\frac{V_o}{V}\right)^{2/3} - 1\right]^2\left[6 - 4\left(\frac{V_o}{V}\right)^{2/3} - 1\right]\right\} \quad (11)$$

Here, the optimized parameters E_o B_o, V_o and B_o' represent total energy, bulk modulus, equilibrium volume, and pressure derivative, respectively in the stress-free state.

Goldschmidt's rule for the effective ionic radii [54] has numerous aspects, such as volume optimization that determine the structural stability of the materials. Density functional theory-based simulation code (WIEN2K) is used to perform the geometrical optimization for both studied compounds. The crystal structure of both compounds and their volume optimization curves are shown in Fig. 1.

The formation energy (E_F) is used to predict the stability of the compound. E_F highlights the difference between the compound's optimized energy and the energy of its inherent atoms in their model reference states [55].

The formation energy (E_F) is calculated by using the following relation.

$$E_f^{Rb2TlInX6} = E_{total}^{Rb2TlInX6} - 2E_{Rb} - E_{Tl} - E_{In} - 6E_{X=Cl,\ I} \quad (12)$$

Where $E_{total}^{Rb2TlInX6}$ is the total ground state energy and E_{Rb}, E_{Tl}, E_{In} *and* E_X are the total energies of the constituent elements. The positive E_F means that the material shows unstable behavior and the negative E_F verifies the stability of the material [56].

A detailed theoretical analysis regarding the stability of both compounds $Rb_2TlInCl_6$ and Rb_2TlInI_6 was done. Goldschmidt Tolerance Factor (τ_G) and Octahedral factor (μ) are considered essential parameters in order to maintain stability as well as to examine the formation of perovskites and can be determined with the following relations:

$$\tau_G = \frac{R_A + R_X}{\sqrt{2}(R_B + R_X)} \quad (13)$$

And

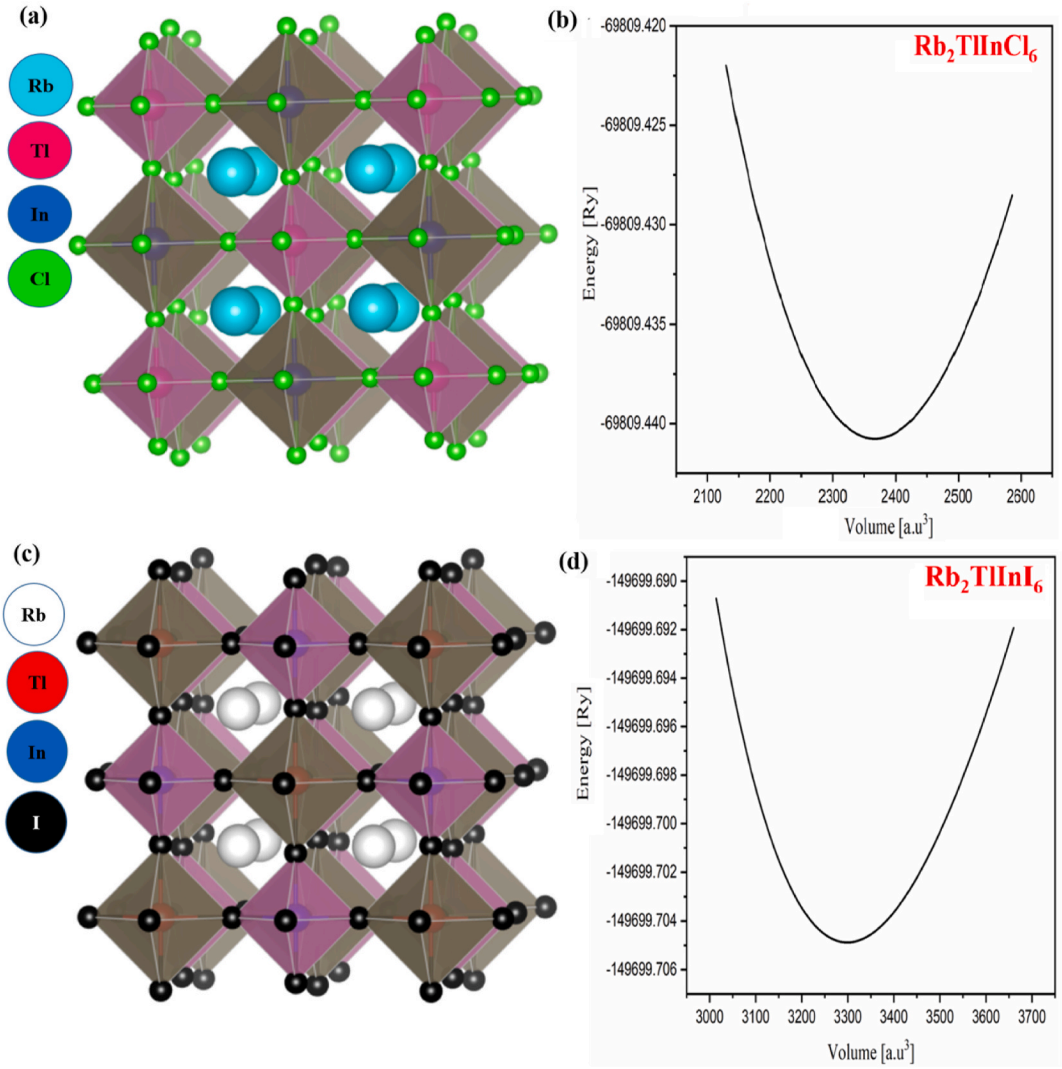

Fig. 1. Crystal structure and optimization plot for $Rb_2TlInCl_6$ and Rb_2TlInI_6 compounds.

$$\mu = \frac{R_B}{R_X} \tag{14}$$

Where R_A, R_B and R_X are Shannon ionic radii of elements.

In a 3D framework, the double perovskite structure has an octahedral arrangement of $B^{'}$ X_6 and B'' X_6. So,

$$R_B = \frac{R_{B'} + R_{B''}}{2} \tag{15}$$

The tolerance factor within the range of $0.8 < \tau_G < 1.0$ allows the formation of the perovskite structure and is favourable for cubic structure, the calculated tolerance factor values fall in the given range for both compounds as presented in Table 1, which confirms their cubic structures.

The octahedral factor envisages the formation and distortion of the crystalline structure in vacancy-ordered double perovskites $A_2BB^{'}X_6$ [57]. If the octahedral factor is within the range of $0.29 < \mu < 0.55$, $A_2BB^{'}X_6$ stabilizes in the cubic phase at room temperature. In Table 1, the octahedral factor decrease on going from X = Cl to X = I, because the ionic radius of the halogen anion increases, due to this, the perovskite structure undergoes octahedral tilting and then its symmetry becomes lowered from the cubic structure to a lower-symmetry structure at room temperature. According to previous experiments [58,59], the calculated octahedral factor (μ) is 0.47 and 0.39 for $Rb_2TlInCl_6$ and Rb_2TlInI_6, respectively and can be concluded that it crystallizes in the stable cubic phase at room temperature.

The calculated optimization parameters like equilibrium volume (V_0), lattice constant (a_0), bulk modulus (B), pressure derivatives of bulk modulus ($B^{'}$), ground state energy (E_0), and formation energy E_f for these double perovskites compounds are mentioned in Table 1.

For most materials, the bulk modulus does change with pressure and this behavior is captured by the pressure derivative of the bulk modulus i.e., B′ value. Values of bulk modulus and B′ are pressure dependent, and empirical formulations for the equation of states use the values for density, bulk modulus, and B′ at zero pressure as parameters.

The E-V curve communicates the minimum energy at the ground state.

3.2. Elastic properties

To assess the stability and find out the capability of a material to withstand the application of force is determined by the essential parameter, known as elastic constant. The measurement of an elastic constant is a key step to identify the mechanical stability, ductility and type of bonding forces. In this report, the value of elastic constants C_{ij} (C_{11}, C_{12}, C_{44}) is computed by using the relation of strain as a function of volume [30] and discussed in Table 2. The Thomas Charpin method [60] is applied to find out the elastic constant values C_{ij} (C_{11}, C_{12}, C_{44}). If a crystal has a cubic symmetry, the stability criteria is presented [61] as,

$$(C_{11} - C_{12}) > 0,\ C_{11} > 0,\ C_{44} > 0,\ (C_{11} + 2C_{12}) > 0,\ C_{12} < B < C_{11} \tag{16}$$

The above-mentioned parameters are effectively taken by the estimated elastic constant values and provided in Table 2. Both compounds' elastic constants are positive and follow the Born stability criteria condition [62]. Mechanical properties such as the physical toughness of the material, nature of bonding forces, material stiffness and the plastic twist of the material have been studied by the Young modulus (Y), Poisson ratio (ν), Bulk modulus (B) and Shear modulus (G). The estimated values of elastic constant by the mean of Voigt-Reuss- Hill approximation [63,64] are discussed in Table 2. The following equations represent the calculated parameters.

Table 2
Calculated elastic constants (C_{11}, C_{12}, C_{44}) in (GPa), Bulk Modulus B (GPa), Shear Modulus G (GPa), B/G ratio, Young's modulus Y(GPa), Poisson's ratio (ν), Zener anisotropy factor (A^u) and Cauchy pressure (C_{12}–C_{44}) for $Rb_2TlInCl_6$ and Rb_2TlInI_6.

Parameters	$Rb_2TlInCl_6$	Rb_2TlInI_6	$Cs_2AgBiCl_6$ [70]
C_{11} (GPa)	48.53	68.59	50.03
C_{12} (GPa)	12.66	14.78	19.96
C_{44} (GPa)	2.02	4.70	7.76
Bulk modulus (B in GPa)	24.68	16.51	29.98
Shear modulus (G in GPa)	5.75	10.30	10.14
Pugh's ratio (B/G)	4.29	1.60	2.96
Young modulus (Y)	16.00	25.57	27.35
Poisson's ratio (ν)	0.39	0.24	0.35
Zener anisotropy factor (A^u)	0.11	0.17	–
Cauchy pressure	10.64	10.08	–

$$G_V = \frac{1}{5}(C11 - C12 + 3C44) \tag{17}$$

$$G_R = \frac{5(C11 - C12)C44}{3(C11 - C12) + 4C44} \tag{18}$$

G_V and G_R are Voigt's and Reuss's Shear moduli.

An isotropic factor 'A' determines the characteristic of elastic, magnetic and electronic properties in various structure directions. The material shows the isotropic behavior if A = 1 and deviation from '1' represents the anisotropic behavior [65].

$$A = \frac{2C44}{C11 - C12} \tag{19}$$

A is Zener anisotropy factor, The calculated elastic constants values for $Rb_2TlInCl_6$ and Rb_2TlInI_6 are 0.11 and 0.17, respectively, deviating from unity and showing that both materials have anisotropic behavior.

The bonding forces between the individual atoms are described by Poisson's ratio (ν).

$$\nu = \frac{3B - 2G}{2(3B + G)} \tag{20}$$

The materials having covalent, ionic and metallic bonding take the value of 0.1, 0.25 and 0.33, respectively [66,67]. The calculated poisson's ratio for $Rb_2TlInCl_6$ shows that it has metallic bonding while Rb_2TlInI_6 possesses ionic bonding.

Many existing theories try to predict the plastic behavior of materials, no doubt due to the ease with which elastic constants can be measured is that of the Pugh Ratio. The Pugh ratio (B/G), where B is the bulk modulus and G is the shear modulus, represents the plasticity and fracture. If plasticity is easier, then the material will tend to be ductile, whereas if fracture is easier, then the material will tend to be brittle. The Pugh's ratio gives evidence that the material is ductile or brittle [68]. If the B/G ratio is less than 1.75, the material shows the brittle nature and greater than 1.75 shows the ductile nature. The calculated B/G ratio shows that $Rb_2TlInCl_6$ possesses a ductile nature and Rb_2TlInI_6 is brittle. The material's ductility or brittleness can be determined by the Cauchy pressure [69]. The Cauchy pressure (C_{12}–C_{44}) describes the elastic constants in terms of the single crystal of a cubic material and is used to determine the nature of the bonding in a material. The materials with

Table 1
Optimized lattice parameters for $Rb_2TlInCl_6$ and Rb_2TlInI_6 compoumds

Compound	Lattice Constant	V_0 (a.u^3)	B(GPa)	$\mathbf{B^{'}}$ **(GPa)**	$E_0(R_Y)$	E_F (eV/atom)	Tolerance factor	Octahedral factor
$Rb_2TlInCl_6$	11.20Å	2367.1987	24.68	3.0558	−69809.440765	−2.042	0.89	0.47
Rb_2TlInI_6	12.50Å	3298.9150	16.51	7.8011	−149699.704881	−1.125	0.86	0.39

metallic bonding exhibit a positive Cauchy pressure. The covalent bonding in solids is depicted with negative Cauchy pressure values, i.e., C44 > C12. Moreover, the Cauchy pressure (C_{12}–C_{44}) helps in examining a material's ductility and brittleness. The positive value shows ductility and the negative value shows the brittle nature of the material. Both studied compound shows a ductile nature because of positive values of Cauchy Pressure.

The amount of material's stiffness is determined by Young's modulus. The greater value of Young's modulus, the more stiffness and greater resistance to deformation results in increasing the strength of the material. The large value of Bulk modulus (B) shows the greatest resistance of the material to volumetric change under the influence of external pressure.

$$G = \frac{G_V + G_R}{2} \tag{21}$$

and,

$$Y = \frac{9BG}{3B + G} \tag{22}$$

Where 'G', 'B,' and 'Y' known as Shear, Bulk, and Young Modulus respectively.

Table 2 contains all of the computed elastic constants and mechanical properties. We couldn't find any elastic or mechanical data for this compound in the literature, but our findings are comparable to other double oxide perovskites [38,66,71–73].

3.3. Electronic properties

The electronic properties of a material, such as its band structure and the distribution of electrons within these bands significantly impact its applications [74]. We analysed the electronic characteristics of double perovskites using density functional theory in this report. The band structure is estimated using non-spin polarized calculations based on modified Becke-Johnson (mBJ) approximation and Spin-Orbit Coupling (SOC) methods. Fig. 2 (a –d) describes the electronic band profile for both mBJ and mBJ+SOC potentials. It can be seen that the Fermi level is unoccupied, confirming the semiconducting nature of Rb_2TlInX_6 (X = Cl, I). Furthermore, the conduction band maxima (CBM) and valence band minima (VBM) lie at distinct symmetric positions, i.e., (L −*X*) for $Rb_2TlInCl_6$ and Rb_2TlInI_6, resulting in an indirect bandgap. With mBJ potential, an indirect bandgap of 3.51eV and 1.43eV is achieved for $Rb_2TlInCl_6$ and Rb_2TlInI_6, respectively. While using mBJ+SOC, a decrease in the bandgap is observed with new values of 3.49eV for $Rb_2TlInCl_6$ and 1.40eV for Rb_2TlInI_6. The reduction in the bandgap is due to the downshifting and splitting in the conduction band by applying spin-orbit coupling. The total density of states (TDOS) is the number of distinct states that electrons can occupy at a given energy level. The total density of states (TDOS) is used to illustrate the qualitative description of the valence and conduction band, as well as the energy states associated with them. The total density of states (TDOS) is shown in Fig. 2 for Rb_2TlInX_6 (X = Cl, I) with mBJ and mBJ+SOC potentials.

The TDOS also justifies the energy band-gap value and semiconducting nature of Rb_2TlInI_6 and Rb_2TlInI_6 with both potentials. The highest peaks for $Rb_2TlInCl_6$ and Rb_2TlInI_6 show the maximum contribution of Chlorine (Cl) and Iodine (I) in the valence band and Indium (In) and Rubidium (Rb) in the conduction band. The TDOS graphs show good agreement with the band structure results.

The partial density of states (PDOS) provides information about the contribution of individual atoms in the energy levels as presented in Fig. 3. For $Rb_2TlInCl_6$, the Cl-p and Tl-s states have the main contribution in the valence band, while Rb-d and In-p states have the significant contribution in the conduction band with mBJ potential. The Cl-p and Rb-d states show the main contribution in the valence band and Tl-p and In-s states have maximum contribution in conduction band with

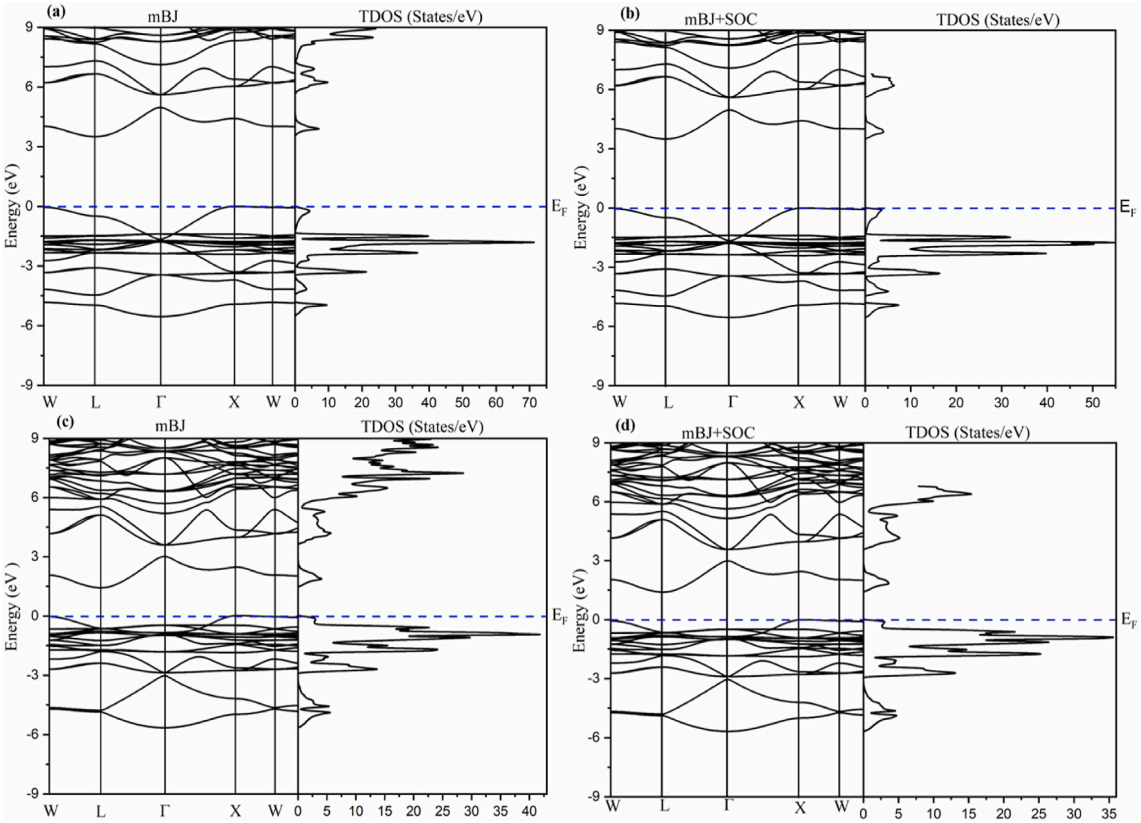

Fig. 2. Calculated bandgap and density of states for $Rb_2TlInCl_6$ (a, b) and Rb_2TlInI_6 (c,d) with mBJ and mBJ+SOC potentials.

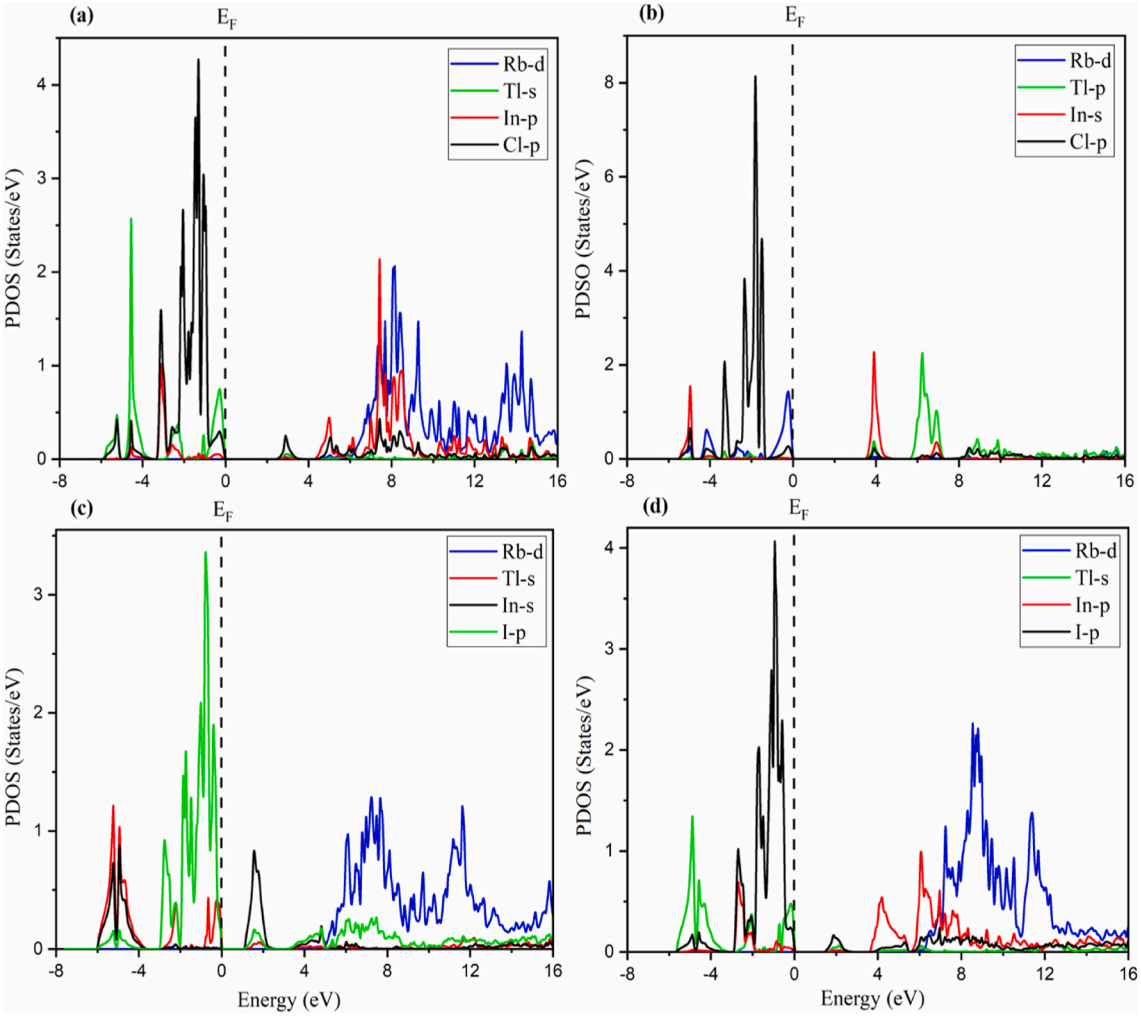

Fig. 3. Partial density of states for $Rb_2TlInCl_6$ (a, b) and Rb_2TlInI_6 (c,d) with mBJ and mBJ+SOC potentials, respectively.

mBJ+SOC potential represented in Fig. 3 (a-b). For Rb_2TlInI_6, the I-p and Tl-s have the main contribution in the valence band, while Rb-d states show the maximum contribution in the conduction band with both potentials as represented in Fig. 3 (c-d).

3.4. Optical properties

The optical characteristics are intrinsically linked to its dielectric function. These qualities are being investigated by looking into their ability to harvest the energy of visible light, which is typically accomplished by determining the energy gap and absorptive behavior [75]. The frequency and optical properties of a material are interrelated because optical properties are frequency-dependent. We can simply extract all other properties by calculating one reliable property, the dielectric constant. The optical parameters like reflectivity R(ω), refractive index n(ω), absorption coefficient α (ω) are derived from the dielectric function ε(ω) [76]. The dielectric function ε(ω) explains the interaction of an incident photon with its constituent atoms and the optical response of a material is described. The isotropic character of the crystal is taken into account for cubic symmetry ($\varepsilon_{xx} = \varepsilon_{yy} = \varepsilon_{zz} = \varepsilon$). The dielectric constant ε(ω) is divided into two parts: the real component $\varepsilon_1(\omega)$ describes the dispersion and polarization of the material and the imaginary part $\varepsilon_2(\omega)$ represents light depletion.

$$\varepsilon(\omega) = \varepsilon_1(\omega) + i\varepsilon_2(\omega) \tag{23}$$

Where

$$\varepsilon_1\left(\omega\right) = 1 + \frac{2p}{\pi}\int_0^{\infty}\frac{\omega'\varepsilon_2(\omega')}{\omega'^2 - \omega^2}d\omega' \tag{24}$$

When polarized materials allow the light to pass at resonance frequency, the maximum dispersion has appeared, which is determined by the positive peaks. The reason for dispersion is the atomic dipoles vibration at the resonance frequency, which allows the light to pass from a single plane.

Fig. 4 shows the dielectric function's real part $\varepsilon_1(\omega)$. In real part $\varepsilon_1(\omega)$ of dielectric constant, the static points are 2.18 and 2.20 for $Rb_2TlInCl_6$ and 3.96 and 3.98 for Rb_2TlInI_6 with mBJ and mBJ+SOC potentials, respectively. The first peak intensity is 3.87 at 4.01eV and 3.81 at 3.92eV for $Rb_2TlInCl_6$ and 6.29 at 2.00eV and 6.26 at 2.00eV for Rb_2TlInI_6 with mBJ and mBJ + SOC potentials, respectively. The intensity of peak decrease uniformly and the second peak is observed at 6.29eV and 6.23eV for $Rb_2TlInCl_6$ and 4.09eV and 4.07eV for Rb_2TlInI_6 with mBJ and mBJ+SOC potentials, respectively. Other peaks are also observed with increased energy, as shown in Fig. 4 (a, b).

The negative portion of the real part $\varepsilon_1(\omega)$ of dielectric function is between 12.75eV to 13.57eV for $Rb_2TlInCl_6$. In the case of Rb_2TlInI_6, the curve reaches the negative value at 8.01eV with mBJ+SOC and it rises again and gets the peak in the positive range. The peak decreases again and achieves negative values from 9.19eV to 13.57eV with both potentials. The negative region is a disallowed region for electromagnetic (EM) waves because the compounds show metallic behavior in this

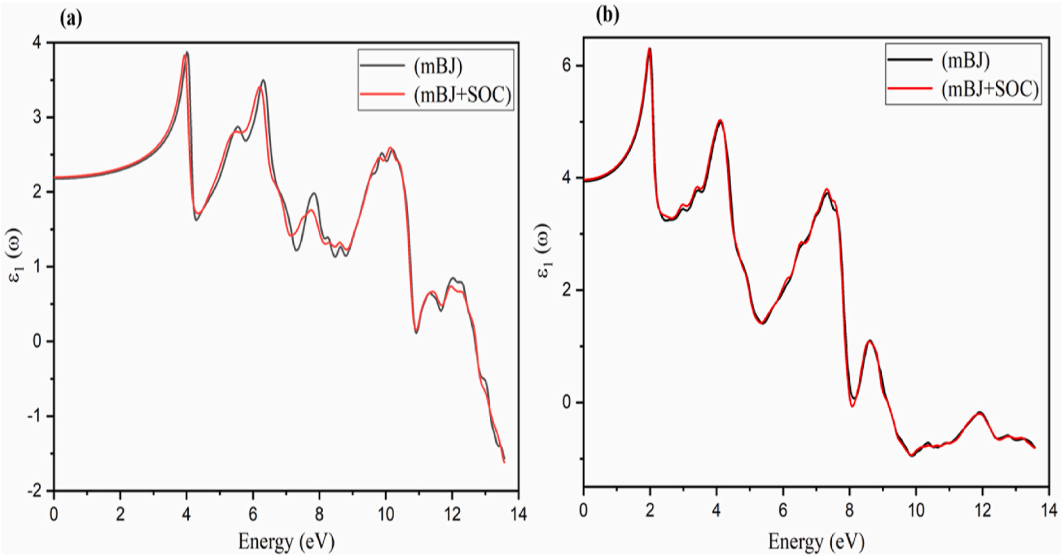

Fig. 4. Real part of dielectric constant for $Rb_2TlInCl_6$ (a) and for Rb_2TlInI_6 (b) with mBJ and mBJ+SOC potentials.

region. Penn's model, ε_1 (*0*) ≈ 1+ ($\hbar\omega_p$/Eg) [77] which represent the condition for dielectric function ε_1 (0) >1, is used to determine the values of $\varepsilon_1(0)$ and E_g for both semiconductors.

The $\varepsilon_2(\omega)$ provides information about the absorption of light and penetration depth and is directly related to the electronic band gap and describes the electron transitions from the valence band to the conduction band. As the photon energy increases, the transition from valence (mostly p-orbitals) to the conduction band (p and d-orbitals) occurs and represents the first peak for both compounds. The second peak also corresponds to such transitions. The plots in Fig. 5 show the critical values of $\varepsilon_2(\omega)$ and indicate the optical bandgaps of the studied compounds. According to our calculated results, the optical bandgap is identical to the electronic band structure profile.

Furthermore, light absorption at the energy range of 2.51eV–7eV is a more favourable energy region to use studied compounds in solar cells and optoelectronic devices. Above 8eV ultraviolet regions start, which shows metallic behavior because of minimum absorption.

The refractive index n(ω) influences the efficiency of transparent and dispersion light into its constituent portions and varies with wavelength.

The rate of transparency and dispersion of light is measured by the refractive index n(ω), which is based on its constituent components. In Fig. 6 (a, b), the maximum value of refractive index n(ω) is 1.98 at 4.01eV and 1.96 at 3.97eV for $Rb_2TlInCl_6$ with mBJ and mBJ+SOC potentials, respectively. The maximum value of n(ω) with both potentials is 2.53 at 2.01eV for Rb_2TlInI_6. The above mentioned values determined that the highest refractive index n(ω) value lies in the ultraviolet region for $Rb_2TlInCl_6$ and visible region for Rb_2TlInI_6. Fig. 6 (a, b) shows that the refractive index n(ω) decreases with the increase in energy which shows the inverse relationship between the refractive index n(ω) and the energy. The transparency rate minimizes the refractive index value in high-energy regions due to the metallic response of the materials in this region.

The roughness of surfaces and information about atomic layered are determined by the reflectivity of electromagnetic waves from materials as shown in Fig. 7 (a, b).

The reflectivity starts rising from 0 eV for both compounds and increases with increased energy. The maximum obtained reflectivity is 0.56 at 13.49eV for $Rb_2TlInCl_6$ and 0.60 at 13.57eV for Rb_2TlInI_6 with

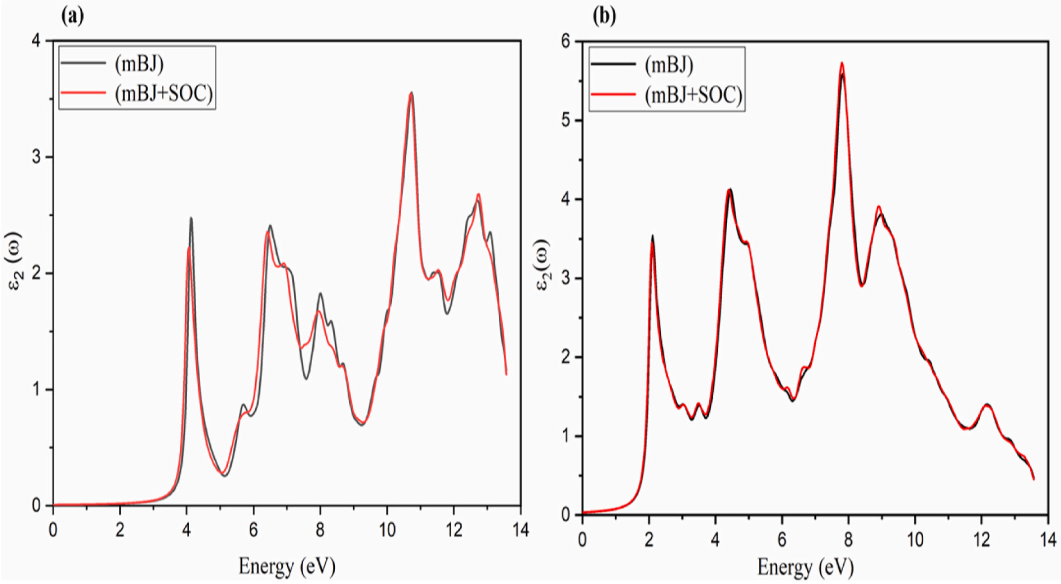

Fig. 5. Imaginary part of dielectric constant for $Rb_2TlInCl_6$ (a) and for Rb_2TlInI_6 (b) with mBJ and mBJ+SOC potentials.

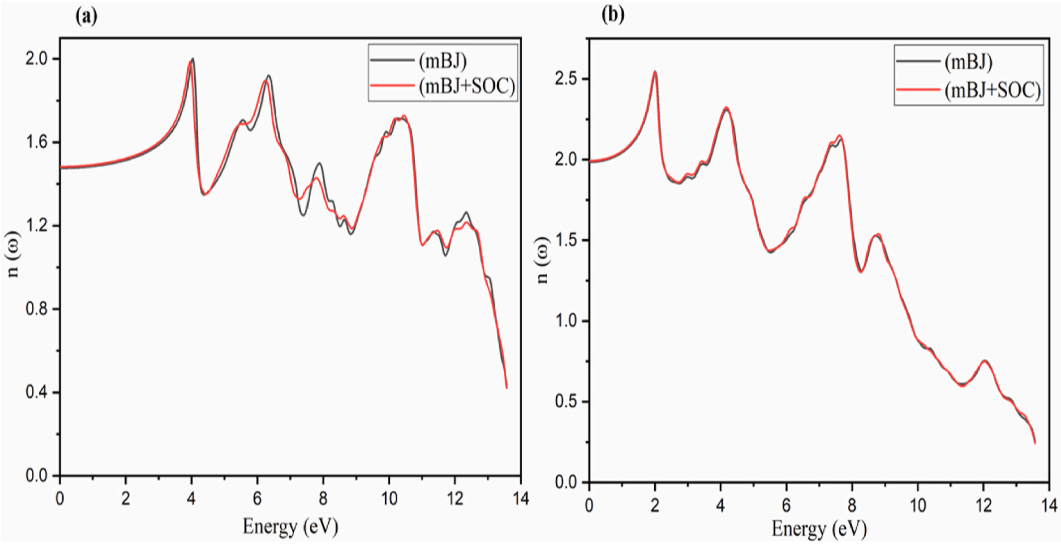

Fig. 6. Refractive index of $Rb_2TlInCl_6$ (a) and Rb_2TlInI_6 (b) with mBJ and mBJ+SOC potentials.

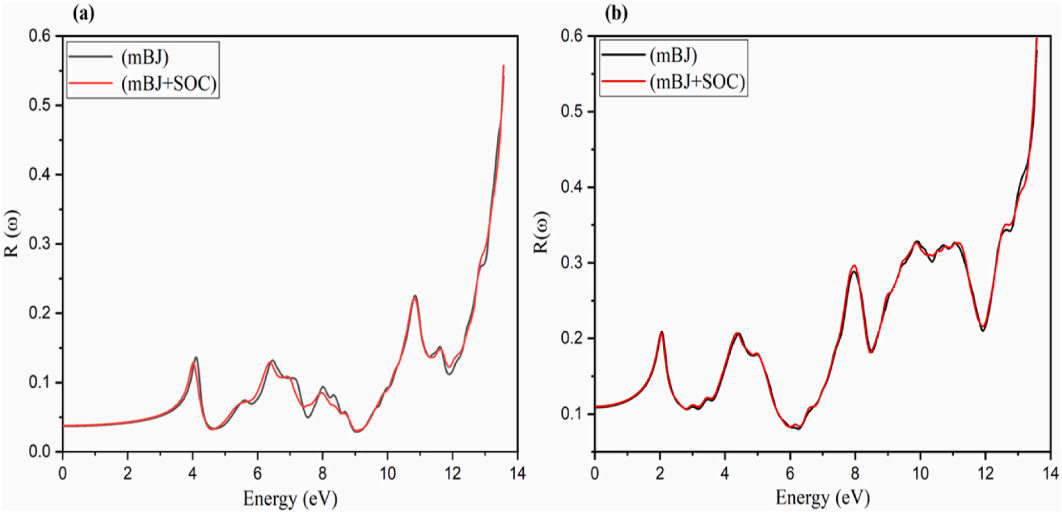

Fig. 7. Reflectivity spectra for $Rb_2TlInCl_6$ (a) and Rb_2TlInI_6 (b) with mBJ and mBJ+SOC potentials.

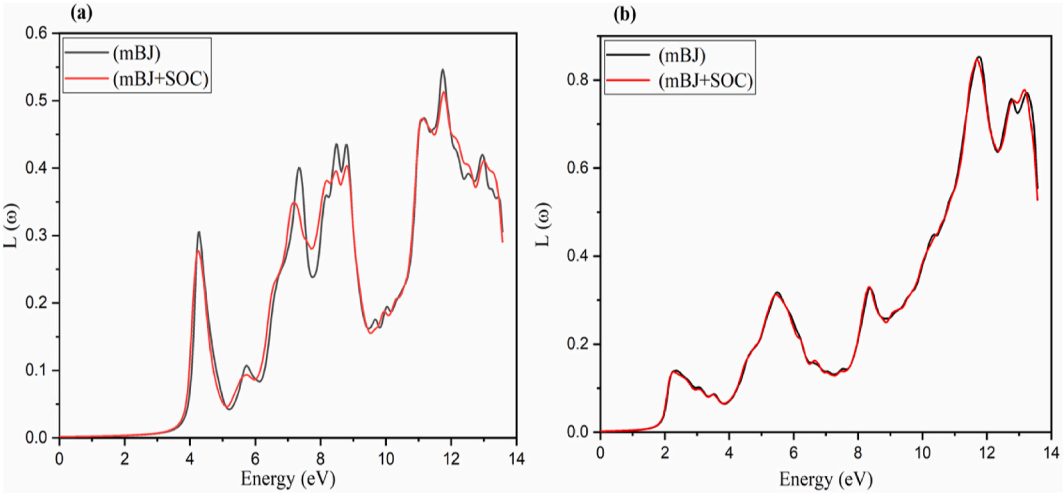

Fig. 8. Calculated optical loss for $Rb_2TlInCl_6$ (a) and Rb_2TlInI_6 (b) with mBJ and mBJ+SOC potentials.

mBJ and mBJ+SOC potentials, respectively. The reflectivity is observed in the high-energy regions that show the low absorption in that region.

The scattering, heating and Plasmon resonance are the main factors of optical loss L(ω). Optical loss measures the energy loss per unit area and is given as.

In Fig. 8 (a, b), the energy loss of electromagnetic waves in the range of 3.5eV–12eV for $Rb_2TlInCl_6$ with maximum peaks of 0.58 with mBJ and 0.5 with mBJ+SOC potential and 1.83eV–11.69eV for Rb_2TlInI_6 with peak value of 0.84 with mBJ and 0.82 with mBJ+SOC potential. The Rb_2TlInI_6 has high optical loss as compared to $Rb_2TlInCl_6$. The calculated energy loss for both compounds is minimal and does not affect the performance of the materials.

The absorption coefficient α (ω) determines how much light can penetrate the material before it completely decays. Every semiconductor material has its threshold limit, below which they do not absorb light. Above this threshold limit, the photon can interact with valence electrons and be able to absorb light. The maximum decay of light is represented by the relation $\alpha = 4\pi k/\lambda$ [78–80]. The calculated values of absorption coefficient α (ω) for both compounds are presented in Fig. 9.

The rate of absorption start from 3.5eV for $Rb_2TlInCl_6$ and 1.73eV for Rb_2TlInI_6. The highest peak values for $Rb_2TlInCl_6$ are 10.71eV and for Rb_2TlInI_6 9.79eV with mBJ and mBJ+SOC potentials respectively. When electrons absorb the energy of the incoming photons with a distinct excitation rate, they produce greater fluctuations in higher energy regions. The relationship between photon and electrons ejects the electrons from valence to conduction band. The extensive study of optical behavior ensures that $Rb_2TlInCl_6$ and Rb_2TlInI_6 are suitable for optoelectronic applications due to the maximum absorption and minimum energy loss.

3.5. Thermoelectric properties

Investigating the dependence of transport properties such as carrier concentration, conductivity, Seebeck coefficient, etc., on temperature is crucial in designing renewable energy devices. To show the influence of transport coefficients at various temperatures, we used the BoltzTraP code [49]. The degree of thermoelectric characteristics in semiconductors is primarily determined by band structure, carrier type, carrier concentration and carrier effective mass, which are all contributing significantly [81]. The energy bands within the Fermi level are intimately linked to transport behavior. In the electronic properties section, it is found that mBJ and mBJ+SOC potentials effectively improve the bandgap values. The bandgap is primarily responsible for determining the carriers (electrons and holes) participating in the transport mechanism. As a result, the bandgap value significantly impacts the transport properties such as conductivity and the Seebeck coefficient. Insulators have a high Seebeck coefficient, whereas metals have a low Seebeck coefficient [82]. Conductivity is proportional to the effective charge carrier. We computed the transport properties using both mBJ and mBJ+SOC to better understand the influence of bandgap on the transport properties.

Fig. 10(a-b) shows the Seebeck coefficient (S) as a function of temperature. The Seebeck coefficient (S) shows noticeable peaks and dips across the temperature range. For $Rb_2TlInCl_6$, at 100K, the Seebeck coefficient value is 2.47×10^{-4} ($V.K^{-1}$) and 2.24×10^{-4} ($V.K^{-1}$) and at 800K, the Seebeck coefficient value is 1.94×10^{-4} ($V.K^{-1}$) and 1.92×10^{-4} ($V.K^{-1}$) with mBJ and mBJ+SOC potentials, respectively. The Seebeck coefficient values show a decrease with the increase in temperature. For Rb_2TlInI_6, at 100K, the Seebeck coefficient value is 9.05×10^{-5} ($V.K^{-1}$) and 2.19×10^{-4} ($V.K^{-1}$) and its value become 1.80×10^{-4} ($V.K^{-1}$) and 2.01×10^{-4} ($V.K^{-1}$) at 800K with mBJ and mBJ+SOC potentials, respectively.

By increasing the temperature, the carrier (electrons and holes) concentration increases gradually, resulting in a decreased Seebeck coefficient (S) value.

The electrical conductivity (σ), which depends upon the density of charge carriers, is one of the most important thermoelectric parameters. Fig. 11 displays the temperature dependent electrical conductivity (σ/τ) for both compounds with mBJ and mBJ+SOC potentials.

It is noted that uniform growth is observed in electrical conductivity by increasing the temperature. The reason is the enhancement in the carrier's mobility and concentration in the conduction band as there is a direct relationship between electrical conductivity and temperature [83].

Thermal conductivity is the ability of a material to conduct heat due to lattice vibrations. The thermal conductivity is the sum of electronic components (K_e) and lattice conductivity (K_l) and mathematically can be written as $K_{el} = K_e + K_l$. The calculated electronic part is corresponds to the electron and holes that transport heat. The thermal conductivity (K_{el}/τ) is plotted as a function of temperature, as shown in Fig. 12. From the figure, it can be seen that K_{el} is rapidly increased by increasing the temperature.

In the case of $Rb_2TlInCl_6$, the thermal conductivity remain the same for both potentials with increasing the temperature and it has a value of 6.63×10^{13} W/mK at 300K. For Rb_2TlInI_6, it has values of 5.35×10^{13} W/mK and 7.13×10^{13} W/mK at 300K with mBJ and mBJ+SOC

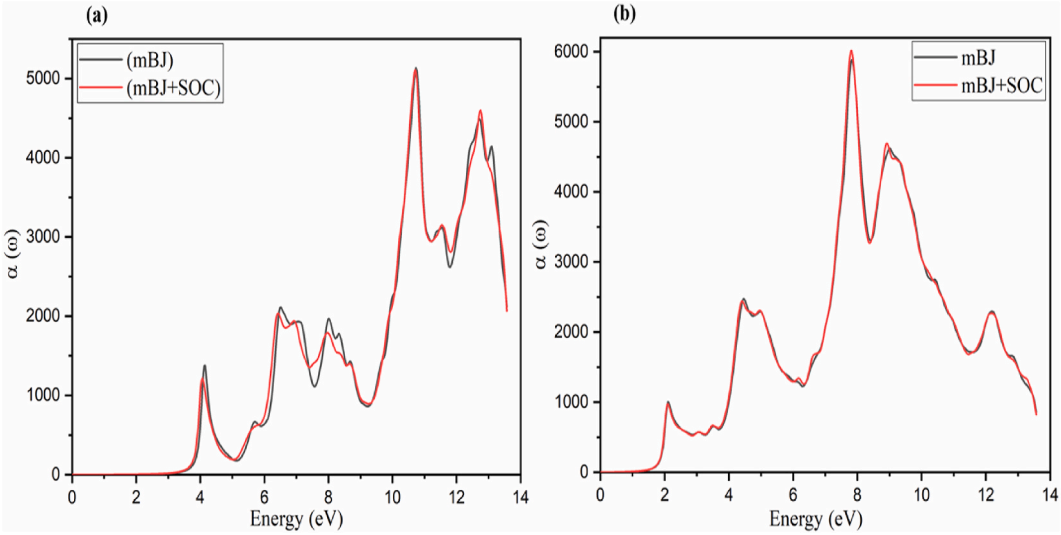

Fig. 9. Calculated absorption coefficient for $Rb_2TlInCl_6$ (a) and Rb_2TlInI_6 (b) with mBJ and mBJ+SOC potentials.

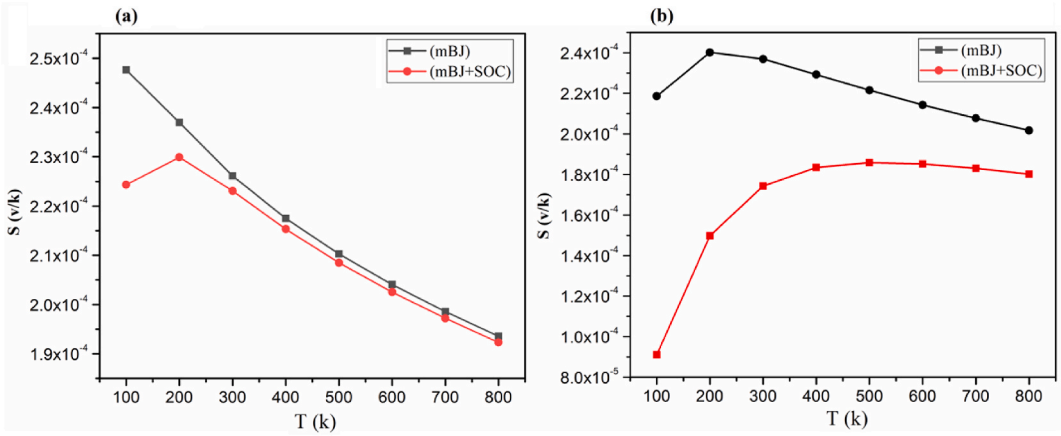

Fig. 10. Seebeck coefficient (S) of $Rb_2TlInCl_6$ (a) and Rb_2TlInI_6 (b) with mBJ and mBJ+SOC potentials.

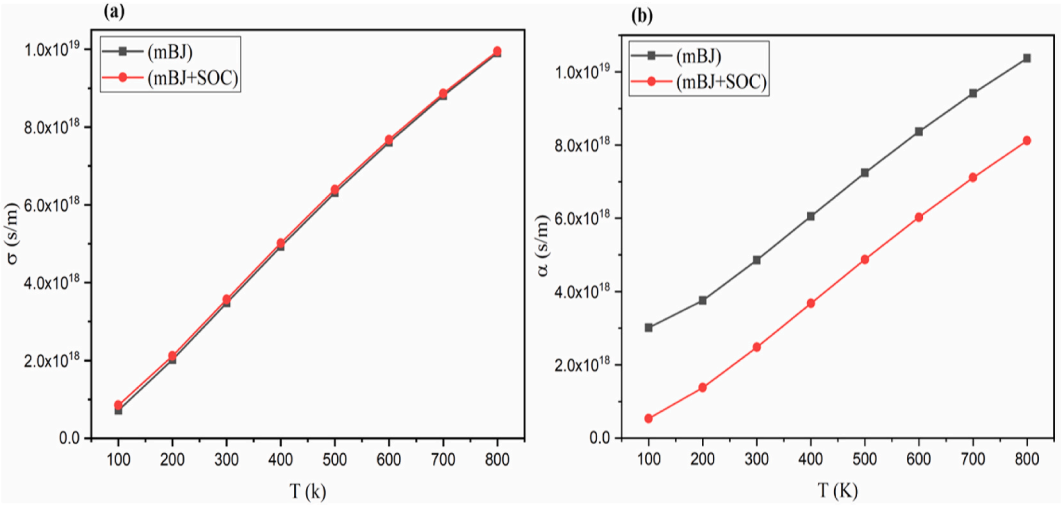

Fig. 11. Electrical conductivity (σ) of $Rb_2TlInCl_6$ (a) and Rb_2TlInI_6 (b) with mBJ and mBJ+SOC potentials.

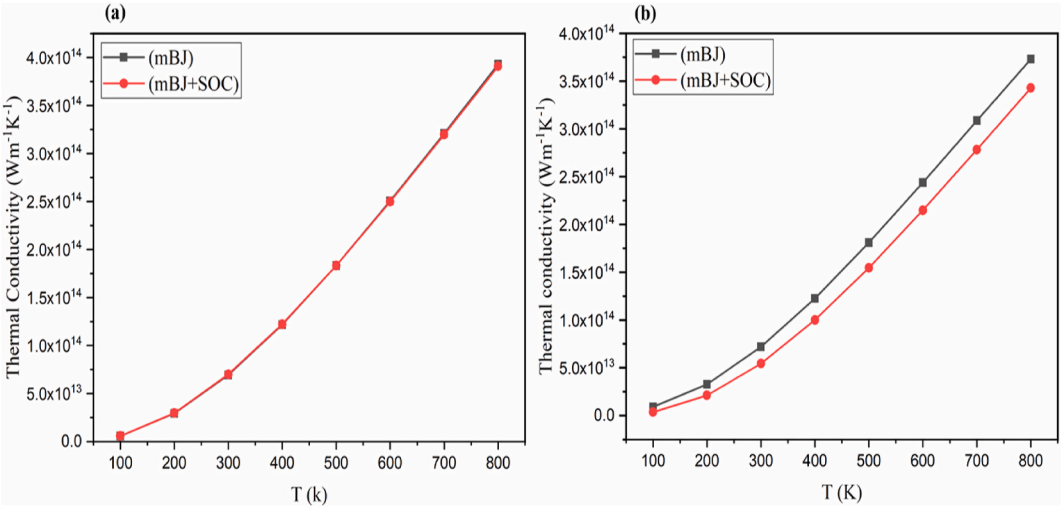

Fig. 12. Thermal conductivity for $Rb_2TlInCl_6$ (a) and Rb_2TlInI_6 (b) with mBJ and mBJ+SOC potentials.

potentials, respectively. The calculated values at room temperature suggest that these are suitable for thermoelectric applications [84].

The power factor (P.F) of thermoelectric material is an essential factor for correctly determining its thermoelectric potency. It can be written as $P.F = S^2\sigma/\tau$, indicating that this property is solely determined by the Seebeck coefficient and electrical conductivity. Fig. 13 represent the power factor as a function of temperature gradient for both compounds with respective potentials.

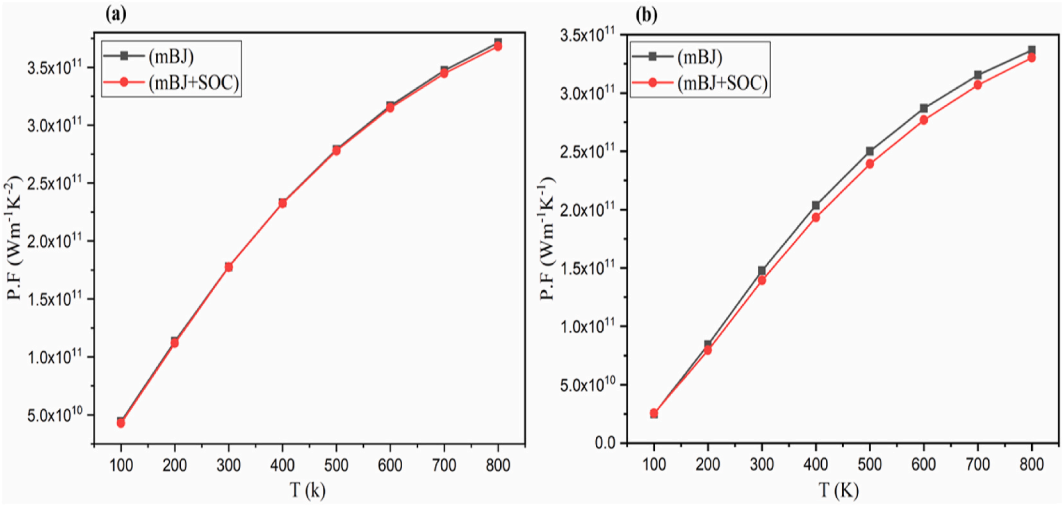

Fig. 13. Power factor for $Rb_2TlInCl_6$ (a) and Rb_2TlInI_6 (b) with mBJ and mBJ+SOC potentials.

The power factor for both compounds increases gradually with raising the temperature from 100K to 800K.

The dimensionless figure of merit (ZT) is the most important parameter for evaluating the efficiency of thermoelectric materials [85]. The ZT value rises while increasing the electrical conductivity and Seebeck coefficient and decreases while increasing the thermal conductivity. Fig. 14 displays the ZT values of both compounds as a function of temperature (100K–800K). For $Rb_2TlInCl_6$, the ZT value shows an increase with temperature (from 100 to 200K for mBJ and 100 to 200K for mBJ+SOC). After 100K for mBJ and 200K for mBJ+SOC, a slight decrease in ZT values is observed for both potentials. A maximum value of 0.755 and 0.753 is achieved at 800K with mBJ and mBJ+SOC potentials, respectively. In the case of Rb_2TlInI_6, the ZT values increase with increasing the temperature for both potentials. A maximum value of 0.72 and 0.77 is obtained with mBJ and mBJ+SOC potentials, respectively.

The moderate values of ZT at high temperatures show the possibility of using the studied perovskites in future thermoelectric devices.

4. Conclusion

Precisely calculated properties of double perovskites Rb_2TlInX_6 (X = Cl, I) are investigated with full-potential linearized augmented plane wave (FP-LAPW) method performed via WIEN2k code. The elastic constants for both compounds are calculated, showing the nature and mechanical stability of both compounds. The mechanical profile reveals that $Rb_2TlInCl_6$ is ductile and Rb_2TlInI_6 is brittle and anisotropic. The band structure and density of states confirmed the semiconducting behavior of studied compounds. The calculated optical parameters are favourable in the ultraviolet region for both compounds, which show their availability for laser applications. The high electrical conductivity and low thermal conductivity are achieved for the studied compounds. The figure of the merit (ZT) shows very good values at room and high temperatures. The optical and transport parameters make these compounds potential candidates for future optoelectronic and thermoelectric applications.

CRediT authorship contribution statement

Moeen Ud Din: Writing – original draft, Software, Methodology, Data curation, Conceptualization. **Quratul Ain:** Validation, Resources, Data curation. **Masood Yousaf:** Visualization, Investigation. **Junaid Munir:** Writing – review & editing, Supervision.

Declaration of competing interest

The authors declare that they have no known competing financial interests or personal relationships that could have appeared to influence the work reported in this paper.

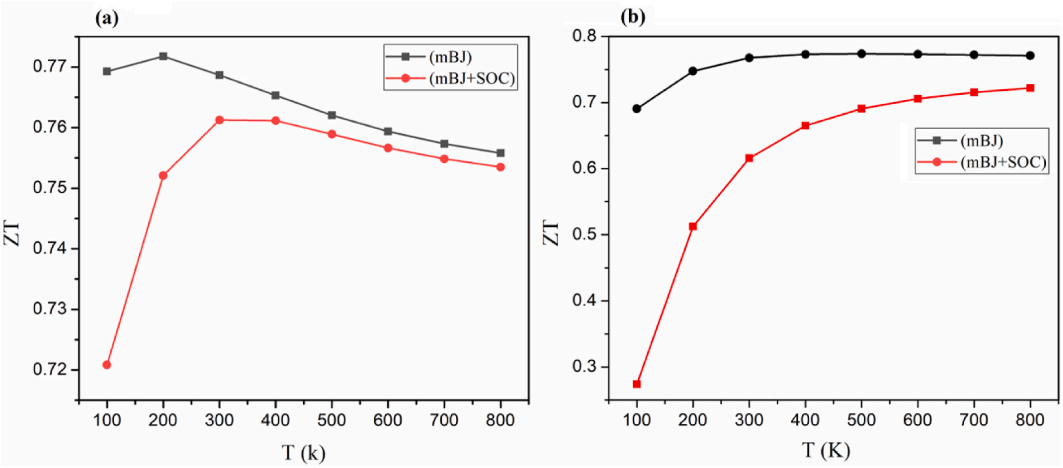

Fig. 14. Figure of merit (ZT) for $Rb_2TlInCl_6$ (a) and Rb_2TlInI_6 (b) with mBJ and mBJ+SOC potentials.

Data availability

Data will be made available on request.

References

[1] G. Pilania, et al., Finding new perovskite halides via machine learning, Front Mater. 3 (2016) 19.
[2] E.A.J. Moore, Computational modelling of inorganic solids, Annual Rep. Sec. Inorganic Chem. 104 (2008) 46–63.
[3] M.U. Din, et al., Electronic structure and optical response of double perovskite Rb2NaCoF6 for optoelectronic devices, Phys. B Condens. Matter 627 (2022), 413533.
[4] A.S. Jbara, et al., Pressure effect on structures and optoelectronic attributes of mixed halide CsPb (I/Br) 3: a density functional theory study, J. Opt. Soc. Am. 38 (7) (2021) 940–946.
[5] A.S. Jbara, et al., Density functional theory study of mixed halide influence on structures and optoelectronic attributes of CsPb (I/Br) 3, Appl. Opt. 59 (12) (2020) 3751–3759.
[6] G. Longo, et al., Understanding the performance-limiting factors of Cs2AgBiBr6 double-perovskite solar cells, ACS Energy Lett. 5 (7) (2020) 2200–2207.
[7] W. Zhu, et al., Low-dose real-time X-ray imaging with nontoxic double perovskite scintillators, Light Sci. Appl. 9 (1) (2020) 1–10.
[8] P. Zhang, J. Yang, S.-H. Wei, Manipulation of cation combinations and configurations of halide double perovskites for solar cell absorbers, J. Mater. Chem. 6 (4) (2018) 1809–1815.
[9] P. Han, et al., Lead-free sodium–indium double perovskite nanocrystals through doping silver cations for bright yellow emission, Angew. Chem. 131 (48) (2019) 17391–17395.
[10] K.-I. Kobayashi, et al., Room-temperature magnetoresistance in an oxide material with an ordered double-perovskite structure, Nature 395 (6703) (1998) 677–680.
[11] M. Iliev, P. Padhan, A.J.P.R.B. Gupta, Temperature-dependent Raman study of multiferroic Bi 2 NiMnO 6 thin films, Phys. Rev. B 77 (17) (2008), 172303.
[12] M. Fiebig, et al., Observation of coupled magnetic and electric domains, Nature 419 (6909) (2002) 818–820.
[13] H. Das, M. De Raychaudhury, T.J.A.P.L. Saha-Dasgupta, Moderate to large magneto-optical signals in high T c double perovskites, Appl. Phys. Lett. 92 (20) (2008), 201912.
[14] Y. Krockenberger, et al., Sr 2 Cr Os O 6: end point of a spin-polarized metal-insulator transition by 5 d band filling, Phys. Rev. B 75 (2) (2007), 020404.
[15] H.L. Feng, et al., High-temperature ferrimagnetism driven by lattice distortion in double perovskite Ca2FeOsO6, J. Am. Chem. Soc. 136 (9) (2014) 3326–3329.
[16] K. Cao, et al., MAPbI 3− x Br x mixed halide perovskites for fully printable mesoscopic solar cells with enhanced efficiency and less hysteresis, Nanoscale 8 (16) (2016) 8839–8846.
[17] L.-C. Chen, C.-Y.J. Weng, Optoelectronic properties of MAPbI 3 perovskite/titanium dioxide heterostructures on porous silicon substrates for cyan sensor applications, Nanoscale Res. Lett. 10 (1) (2015) 1–5.
[18] J. Ding, et al., Polarization-dependent optoelectronic performances in hybrid halide perovskite MAPbX3 (X= Br, Cl) single-crystal photodetectors, ACS Appl. Mater Interface. 10 (1) (2018) 845–850.
[19] M.A. Najeeb, et al., Growth of MAPbBr3 perovskite crystals and its interfacial properties with Al and Ag contacts for perovskite solar cells, Opt. Mater. 73 (2017) 50–55.
[20] S.A. Dar, et al., Insight into structural, electronic, magnetic, mechanical, and thermodynamic properties of actinide perovskite BaPuO 3, J. Supercond. Nov. Magnetism 31 (10) (2018) 3201–3208.
[21] S.A. Dar, et al., First-principles investigation on electronic structure, magnetic, mechanical and thermodynamic properties of SrPuO3 perovskite oxide, Mater. Res. Express 5 (2) (2018), 026106.
[22] S.A. Dar, et al., A DFT study on structural, electronic mechanical and thermodynamic properties of 5f-electron system BaAmO 3, J. Supercond. Nov. Magnetism 31 (1) (2018) 141–149.
[23] S.A. Dar, et al., A first-principles calculation on structural, electronic, magnetic, mechanical, and thermodynamic properties of SrAmO 3, J. Supercond. Nov. Magnetism 30 (11) (2017) 3055–3063.
[24] K.E. Stitzer, M.D. Smith, H.-C.J. zur Loye, Crystal growth of Ba2MOsO6 (M= Li, Na) from reactive hydroxide fluxes, Solid State Sci. 4 (3) (2002) 311–316.
[25] T. Aharen, et al., Magnetic properties of the geometrically frustrated S= 1 2 antiferromagnets, La 2 LiMoO 6 and Ba 2 YMoO 6, with the B-site ordered double perovskite structure: evidence for a collective spin-singlet ground state, Phys. Rev. B 81 (22) (2010), 224409.
[26] M.A. de Vries, A. Mclaughlin, J.-W.J. Bos, Valence bond glass on an fcc lattice in the double perovskite Ba 2 YMoO 6, Phys. Rev. Lett. 104 (17) (2010), 177202.
[27] J. Carlo, et al., Triplet and in-gap magnetic states in the ground state of the quantum frustrated fcc antiferromagnet Ba 2 YMoO 6, Phys. Rev. B 84 (10) (2011), 100404.
[28] C. Wiebe, et al., Spin-glass behavior in the S= 1/2 fcc ordered perovskite Sr 2 CaReO 6, Phys. Rev. B 65 (14) (2002), 144413.
[29] M.U. Din, et al., Electronic structure and optical response of double perovskite Rb2NaCoF6 for optoelectronic devices, Phys. B Condens. Matter (2021), 413533.
[30] S.A. Dar, V. Srivastava, U.K.J. Sakalle, A combined DFT and post-DFT investigation on cubic XMoO3 (X= Sr, Ba) perovskite oxides, Mater. Res. Express 4 (8) (2017), 086304.
[31] S. Zhao, Z. Wei, S.A.J. Dar, Insight into the structural, electronic, elastic, mechanical, and thermodynamic properties of XReO3 (X= Rb, Cs, Tl) perovskite oxides: a DFT study, Z. Naturforsch. 74 (9) (2019) 827–836.
[32] S.A. Dar, V. Srivastava, U.K.J. Sakalle, High pressure and high temperature investigation of metallic perovskite SnTaO 3, J. Mol. Model. 24 (3) (2018) 1–8.
[33] S.A. Dar, V. Srivastava, U.K.J. Sakalle, Ab initio high pressure and temperature investigation on cubic PbMoO 3 perovskite, J. Electron. Mater. 46 (12) (2017) 6870–6877.
[34] C. Marjerrison, et al., Magnetic ground states in the three O s 6+(5 d 2) double perovskites B a 2 M Os O 6 (M= Mg, Zn, and Cd) from Néel order to its suppression, Phys. Rev. B 94 (13) (2016), 134429.
[35] S.A. Dar, V. Srivastava, U.K.J. Sakalle, Ab-initio DFT based investigation of double perovskite oxide Ba2CdOsO6 with cubic structure, Comput. Condense Mater. 18 (2019), e00351.
[36] A. Bekhti-Siad, et al., Behavior of the Cubic Double Perovskite Compound Pb2FeTaO6 through Mechanical, Electronic and Magnetic Properties via Ab-Initio Calculations, Research Square, 2020.
[37] B. Merabet, et al., Optimal bandgap of double perovskite La-substituted Bi2FeCrO6 for Solar Cells: an ab initio GGA+ U Study, Chin. Phys. Lett. 34 (1) (2017), 016101.
[38] S.A. Dar, et al., Structural, elastic, mechanical, electronic, magnetic, thermoelectric and thermodynamic investigation of half metallic double perovskite oxide Sr2MnTaO6, J. Magn. Magn Mater. 484 (2019) 298–306.
[39] O. Sahnoun, et al., Magnetic and thermoelectric properties of ordered double perovskite Ba2FeMoO6, J. Alloys Compd. 714 (2017) 704–708.
[40] S.A. Dar, et al., Investigation on the electronic structure, optical, elastic, mechanical, thermodynamic and thermoelectric properties of wide band gap semiconductor double perovskite Ba 2 InTaO 6, RSC Adv. 9 (17) (2019) 9522–9532.
[41] M. Faizan, et al., Structural, elastic, electronic and magnetic properties of Ba 2 XOsO 6 (X= Li, Na, Ca) double perovskites, Indian J. Phys. 90 (11) (2016) 1225–1231.
[42] I. Khan, et al., Elastic and optoelectronic properties of Cs2NaMCl6 (M= in, Tl, Sb, Bi), J. Electron. Mater. 50 (2) (2021) 456–466.
[43] M. Saeed, et al., First-principles prediction of the ground-state crystal structure of double-perovskite halides Cs2AgCrX6 (X= Cl, Br, and I), J. Phys. Chem. Solid. 160 (2022), 110302.
[44] M. Saeed, et al., Optoelectronic and elastic properties of metal halides double perovskites Cs 2 InBiX 6 (X= F, Cl, Br, I), Chin. Opt Lett. 19 (3) (2021), 030004.
[45] K. Schwarz, P. Blaha, G.K.J. Madsen, Electronic structure calculations of solids using the WIEN2k package for material sciences, Comput. Phys. Commun. 147 (1–2) (2002) 71–76.
[46] J.P. Perdew, K. Burke, M.J.P.r.l. Ernzerhof, Generalized gradient approximation made simple, Phys. Rev. Lett. 77 (18) (1996) 3865.
[47] T. Rezkallah, et al., Investigation of the electronic and magnetic properties of Mn doped ZnO using the FP-LAPW method, Chin. J. Phys. 55 (4) (2017) 1432–1440.
[48] F. Tran, P.J.P.r.l. Blaha, Accurate band gaps of semiconductors and insulators with a semilocal exchange-correlation potential, Phys. Rev. Lett. 102 (22) (2009), 226401.
[49] BoltzTraP G.K. Madsen, D.J.J. Singh, A code for calculating band-structure dependent quantities, Comput. Phys. Commun. 175 (1) (2006) 67–71.
[50] G.K. Madsen, D.J. Singh, A code for calculating band-structure dependent quantities, Comput. Phys. Commun. 175 (1) (2006) 67–71. BoltzTraP.
[51] T. Katsura, Y.J.M. Tange, A simple derivation of the Birch–Murnaghan equations of state (EOSs) and comparison with EOSs derived from other definitions of finite strain, Minerals 9 (12) (2019) 745.
[52] F.J.P.r. Birch, Finite elastic strain of cubic crystals, Phys. Rev. 71 (11) (1947) 809.
[53] F.D. Murnaghan, The compressibility of media under extreme pressures, Proc. Natl. Acad. Sci. USA 30 (9) (1944) 244–247.
[54] S.A. Mir, D.C.J. Gupta, Compounds, Analysis of cage structured halide double perovskites Cs2NaMCl6 (M= Ti, V) by spin polarized calculations, J. Alloys Compd. 854 (2021), 156000.
[55] S.M. Alay-e-Abbas, et al., Evaluation of thermodynamics, formation energetics and electronic properties of vacancy defects in CaZrO 3, Sci. Rep. 7 (1) (2017) 1–15.
[56] A. Kundu, et al., New quaternary half-metallic ferromagnets with large Curie temperatures, Sci. Rep. 7 (1) (2017) 1–15.
[57] U.-G. Jong, C.-J. Yu, Y.-H. Kye, Computational prediction of structural, electronic, and optical properties and phase stability of double perovskites K 2 SnX 6 (X= I, Br, Cl), RSC Adv. 10 (1) (2020) 201–209.
[58] H. Boysen, A.W. Hewat, A neutron powder investigation of the structural changes in K2SnCl6, Acta Crystallogr. Sect. B Struct. Crystallogr. Cryst. Chem. 34 (5) (1978) 1412–1418.
[59] C.J. Howard, B.J. Kennedy, P.M. Woodward, Ordered double perovskites–a group-theoretical analysis, Acta Crystallogr. Sect. B Struct. Sci. 59 (4) (2003) 463–471.
[60] S.A. Dar, et al., Electronic structure, magnetic, mechanical and thermo-physical behavior of double perovskite Ba 2 MgOsO 6, Euro Phyis. J. Plus. 133 (2) (2018) 1–12.
[61] G. Sin'Ko, N.J. Smirnov, Ab initio calculations of elastic constants and thermodynamic properties of bcc, fcc, and hcp Al crystals under pressure, J. Phys. Condens. Matter 14 (29) (2002) 6989.
[62] M. Born, On the Stability of Crystal Lattices. I. In *Mathematical Proceedings Of the Cambridge Philosophical Society*, vol. 36, Cambridge University Press, 1940, pp. 160–172, 2.
[63] R.J. Hill, The elastic behaviour of a crystalline aggregate, Proc. Phys. Soc. 65 (5) (1952) 349.
[64] A.J.M.P. Reuss, Computation of the yield point of mixed crystals due to hiring for single crystals, Math. Phys 9 (1929) 49–58.

[65] V. Tvergaard, J.W.J. Hutchinson, Microcracking in ceramics induced by thermal expansion or elastic anisotropy, J. Am. Ceram. Soc. 71 (3) (1988) 157–166.
[66] S.A. Dar, et al., A combined DFT, DFT+ U and mBJ investigation on electronic structure, magnetic, mechanical and thermodynamics of double perovskite Ba2ZnOsO6, Mater. Sci. Eng., B 236 (2018) 217–224.
[67] J. Haines, J. Leger, G.J. Bocquillon, Synthesis and design of superhard materials, Annu. Rev. Mater. Res. 31 (1) (2001) 1–23.
[68] S.J.T.L. Pugh, Edinburgh, D.P. Magazine, J.o. Science, XCII, Relations between the elastic moduli and the plastic properties of polycrystalline pure metals, he London, Edinburgh, and Dublin Philosophical Magazine and Journal of Science 45 (367) (1954) 823–843.
[69] D. Pettifor, Theoretical predictions of structure and related properties of intermetallics, Mater Sci. Technol. 8 (4) (1992) 345–349.
[70] N. Guechi, et al., Elastic, optoelectronic and thermoelectric properties of the lead-free halide semiconductors Cs 2 AgBi X 6 (X= Cl, Br): ab initio investigation, J. Electron. Mater. 47 (2) (2018) 1533–1545.
[71] Y.-P. Liu, H.-R. Fuh, Y.-K.J.C. Wang, Ab initio research on a new type of half-metallic double perovskites, A2CrMO6 (A= IVA group elements; M= Mo, Re and W), Computation 2 (1) (2014) 12–22.
[72] L. Shi, et al., Structural, elastic, electronic and dynamical properties of Ba 2 MgWO 6 double perovskite under pressure from first principles, Eur. Phys. J. B 86 (1) (2013) 1–8.
[73] M. Nabi, D.C.J.S.R. Gupta, Potential lead-free small band gap halide double perovskites Cs2CuMCl6 (M= Sb, Bi) for green technology, Sci. Rep. 11 (1) (2021) 1–13.
[74] M. Markov, et al., Semi-metals as potential thermoelectric materials, Sci. Rep. 8 (1) (2018) 1–10.
[75] U.-G. Jong, C.-J. Yu, Y.-H.J.R.A. Kye, Computational prediction of structural, electronic, and optical properties and phase stability of double perovskites K 2 SnX 6 (X= I, Br, Cl), RSC Adv. 10 (1) (2020) 201–209.
[76] M. Nabi, T.M. Bhat, D.C.J. Gupta, Effect of pressure on electronic, magnetic, thermodynamic, and thermoelectric properties of tantalum-based double perovskites Ba2MTaO6 (M= Mn, Cr), Int. J. Energy Res. 43 (9) (2019) 4229–4242.
[77] D.R.J.P.R. Penn, Wave-number-dependent dielectric function of semiconductors, Phys. Rev. 128 (5) (1962) 2093.
[78] M. Hassan, A. Shahid, Q.J.S.S.C. Mahmood, Structural, electronic, optical and thermoelectric investigations of antiperovskites A3SnO (A= Ca, Sr, Ba) using density functional theory, Solid State Commun. 270 (2018) 92–98.
[79] Q. Mahmood, et al., Density functional theory-based study of the magnetic and optical properties of PbMO3 (M= Cr, Fe) using the modified BeckeJohnson mBJ functional, J. Phys. Chem. Solid. 128 (2019) 275–282.
[80] M. Rashid, et al., Pressure-Induced modifications in the optoelectronic and thermoelectric properties of MgHfO 3 for renewable energy applications, Arabian J. Sci. Eng. (2021) 1–9.
[81] M. Yaseen, et al., Phase transition and thermoelectric properties of cubic KNbO3 under pressure: DFT approach, J. Mater. Res. Technol. 11 (2021) 2106–2113.
[82] X. Zhang, L.-D. Zhao, Thermoelectric materials: energy conversion between heat and electricity, J.J.o.M 1 (2) (2015) 92–105.
[83] R. Haleoot, B.J. Hamad, Thermodynamic and thermoelectric properties of CoFeYGe (Y= Ti, Cr) quaternary Heusler alloys: first principle calculations, J. Materiomic. 32 (7) (2019), 075402.
[84] K.J.E. Kaur, TiPdSn: a half Heusler compound with high thermoelectric performance, Europhys. Lett. 117 (4) (2017), 47002.
[85] S.A. Mir, D.C.J.S.r. Gupta, Scrutinizing the stability and exploring the dependence of thermoelectric properties on band structure of 3 d-3 d metal-based double perovskites Ba 2 FeNiO 6 and Ba 2 CoNiO 6, Sci. Rep. 11 (1) (2021) 1–13.